Metal-free efficient photocatalyst for stable visible-light photocatalytic degradation of refractory pollutant

Longbo Jiang[a,b], Xingzhong Yuan[a,b,*], Guangming Zeng[a,b], Zhibin Wu[a,b], Jie Liang[a,b], Xiaohong Chen[c], Lijian Leng[a,b], Hui Wang[a,b], Hou Wang[a,b,d,*]

[a] College of Environmental Science and Engineering, Hunan University, Changsha 410082, PR China
[b] Key Laboratory of Environmental Biology and Pollution Control (Hunan University), Ministry of Education, Changsha 410082, PR China
[c] Mobile E-business 2011 Collaborative Innovation Center of Hunan Province, Hunan University of Commerce, Changsha 410205, PR China
[d] School of Chemical and Biomedical Engineering, Nanyang Technological University, Singapore 637459, Singapore

ARTICLE INFO

ABSTRACT

The photocatalytic performance of the star photocatalyst g-C$_3$N$_4$ is restricted by the insufficient solar light absorption, low surface area and the fast recombination of photogenerated electron-hole pairs. The present study developed a facile in situ method to construct hexagonal boron nitride (h-BN) decorated g-C$_3$N$_4$ metal-free heterojunction with the aim to greatly enhance the surface area and promote the charge separation. The physical, chemical and optical properties of the resulted samples were thoroughly characterized. The photocatalytic performance of h-BN/g-C$_3$N$_4$ composites were evaluated under visible light irradiation using antibiotic tetracycline (TC) and rhodamine B (RhB) as target pollutants. Results showed that h-BN/g-C$_3$N$_4$ composites exhibited much higher photocatalytic activity than pure g-C$_3$N$_4$ and h-BN. The optimum photocatalytic efficiency of BC-3 sample for the degradation of TC was about 2.3 and 60.3 times higher than that of individual g-C$_3$N$_4$ and h-BN, respectively. Meanwhile, it was about 7.3 and 11.8 times higher than that of individual g-C$_3$N$_4$ and h-BN for RhB degradation, respectively. The enhanced photocatalytic activity of h-BN/g-C$_3$N$_4$ composite is mainly attributed to the larger surface area and the unique physicochemical properties of h-BN nanosheet which acts as a promoter for photoexcited holes transfer. This work indicates that the metal-free h-BN/g-C$_3$N$_4$ hybrid photocatalyst is a promising material in wastewater control.

1. Introduction

Due to the industrialization and population growth, a large amount of poisonous and hazardous pollutants are produced, which has become a serious environmental problem in many countries [1]. Nowadays, worldwide attention has been drawn to develop the state-of-the-art technologies to degrade toxic and hazardous chemicals in various wastewaters. The most popular Fenton process can generate hydroxyl radicals to completely decompose organic compounds into water and carbon dioxide [2]. However, the traditional Fenton reaction requires large amounts of chemical reagents and suffers from strict pH requirement (pH ~ 3) [3,4]. Recently, much attention has been focused on the photocatalytic strategy for environment purification, as solar energy is an inexhaustible and environmentally friendly energy resource [5–8]. At present, most photocatalysts are metal oxides, sulfides and nitrides with d0 or d10 transition metal cations which have the ability to generate hydroxyl (·OH) and superoxide anion radicals (·O$_2^-$) under light irradiations to degrade or convert pollutants (such as

heavy metals and organic compounds) into environmentally friendly compounds [9–11]. Unfortunately, most of these metal-based catalysts are active only under ultra-violet irradiation which only represents 5% intensity in solar energy, while others absorbing visible light are not stable during the reaction process: for example photocorrosion occurs in metal sulfides [12–14]. Photocatalysts for practical use with relatively high productivity have not yet been found. Searching and optimizing highly efficient photocatalysts is urgently needed.

Recently, metal-free graphitic carbon nitride (g-C$_3$N$_4$) with a visible-light driven band gap and proper band edges has emerged as a new class of photocatalyst [15]. In general, g-C$_3$N$_4$ is typically prepared by the polycondensation of nitrogen-rich organic precursors such as cyanamide, dicyandiamide, guanidine hydrochloride, melamine, urea and thiourea [15–19]. It can exhibit the ability of photocatalytic hydrogen/oxygen evolution from water splitting in the presence of sacrificial reagents and photodegradation of organic pollutants under sunlight irradiation [20,21]. However, it is worth noting that bulk g-C$_3$N$_4$ photocatalyst shows a low photocatalytic activity due to the insufficient

solar light absorption, low surface area and the fast recombination of photogenerated electron-hole pairs. In order to increase the activity, many strategies such as introducing heteroatoms [6], coupling with other semiconductors [22], modified with carbon materials [23], controlling morphology [24] have been used, and g-C3N4-based heterojunction photocatalysts have shown encouraging activity improvement. It is proposed that the increased photocatalytic activity of the heterojunction may be attributed to the effective separation of the photoexcited carriers which are transferred into valence band (VB) and conduction band (CB) of opposite semiconductor respectively due to their potential difference of VB and CB [25,26]. Therefore, scientists have made significant efforts to improve the photocatalytic activity of g-C3N4 by coupling it with other semiconductors, such as TiO2 [22], Bi2O2CO3 [27], ZnIn2S4 [28], Bi4Ti3O12 [29] and Ag3PO4 [30]. In recent years, some two-dimensional carbon materials, such as carbon nanotube, graphene and carbon dots, have been also used as an electron transfer channel for g-C3N4 to accelerate the separation of photoinduced charge carriers and obtain efficient metal-free photocatalysts [4,23,31–34]. Xu et al. prepared a novel multi-walled carbon nanotubes (CNT) modified white C3N4 composite with enhanced visible-light-response photoactivity for methylene blue degradation [31]. The degradation rate of the CNT/white C3N4 photocatalyst is almost 8.1 times as high as that of the white C3N4, which is caused by the efficient separation of the photo-generated charge carriers between C3N4 and CNT. Liao et al. fabricated metal-free graphene-carbon nitride hybrids by sonochemical approach for photodegradation of rhodamine B and 2, 4-dichlorophenol in water [33]. The photodegradation rates are much enhanced due to that the GO acts as a separation centre and electron acceptor in the GO/g-C3N4 hybrid. Fang et al. prepared carbon dots modified g-C3N4 hybrid by using carbon dots and dicyandiamide as precursor, in which carbon dots act as electron-sinks, preventing the recombination of photo-generated electron-hole pairs and thus enhancing the photocatalytic activity of g-C3N4 [23].

Hexagonal boron nitride (h-BN) is also a kind of two-dimensional metal-free material, which is similar to layered-structure graphene and has unique physicochemical properties, such as high stability, non-toxicity, low density and thermal conductivity [35,36]. In the recent researches, h-BN is reported to be a robust substrate for semiconductor photocatalysts [37–42]. More importantly, h-BN will be electronegative when the bulk h-BN is exfoliated into two-dimensional nanosheets. In this study, h-BN powder can be strongly attracted by glass due to the electrostatic interaction. This result confirms that h-BN is electronegative. Furthermore, the negatively charged h-BN nanosheets will attract the photoexcited holes and promote the separation efficiency of photoexcited electron-hole pairs [35,41]. It is different from the above conductive carbon materials (carbon nanotube and graphene) which have also been applied for accelerating the separation of photoinduced charge carriers by serving as an electron transfer channel recently [4,31–34]. Because these carbon materials exhibit high electron mobility and storing capacity, the photocatalytic activity of g-C3N4 can be significantly enhanced by coupling with these carbon materials. However, considering the characteristic recombination time of surface h+ (about 10 ns) is much shorter than that of e− (about 100 ns) [43], increasing the transfer of h+ may be more crucial for the improvement of the photocatalytic activity, especially for the degradation reactions because the oxidation efficiency is usually determined by the number of interfacial holes. Theoretical and experimental work has confirmed that the negatively charged BN derives from stable defects associated with nitrogen vacancies (N edged triangle defects) or carbon impurities [35,37–42]. However, the attempt to construct h-BN nanosheet decorated graphitic carbon nitride as an efficient metal-free photocatalyst for the removal of pollutants has still never been reported.

Herein, we have firstly prepared metal-free h-BN nanosheet/g-C3N4 heterojunction photocatalysts by a facile in-situ growth strategy. The physical, chemical and optical properties of the resulted samples were thoroughly characterized with XRD, XPS, UV–vis DRS, BET, SEM, TEM,

PL, ESR and so on. The photocatalytic performance of h-BN/g-C3N4 composites were evaluated under visible light irradiation using TC and RhB as target pollutants. It could be found that h-BN/g-C3N4 composites showed much higher photocatalytic activity than pure g-C3N4 and h-BN. Furthermore, based on our experimental results, a probable photocatalytic mechanism was also proposed. The key role of h-BN for the improved photocatalytic performance was explored and the main active species were determined.

2. Experimental

2.1. Synthesis of the photocatalysts

All chemical reagents were analytical grade and used without further purification. h-BN powders used in this study were supplied by Chinese Macklin Chemical Reagent Co. The metal-free h-BN nanosheet/g-C3N4 heterojunction photocatalysts were prepared by a facile calcination strategy. Specifically, a certain amount (1.0 g) of dicyandiamide and different amount of h-BN were added into an agate mortar and grounded together. The resultant powders were transferred to a covered crucible, then calcined at 550 °C for 4 h with a heating rate of 10 °C/min [44]. After being cooled to room temperature, the resulting products were collected and milled into powder in an agate mortar for further use. To make clarity, the h-BN/g-C3N4 composites with expected h-BN contents of 1.0, 1.5, 2.0, 4.0, 12, and 20 mg were referred to as BC-1, BC-2, BC-3, BC-4, BC-5 and BC-6, respectively. XPS analysis was used to determine the content of h-BN in the h-BN/g-C3N4 composites. The results indicated that the mass contents of h-BN in BC-1 to BC-6 were 0.25%, 0.37%, 0.48%, 0.99%, 2.28%, and 4.53%, respectively. For comparison, h-BN nanosheet was obtained similarly but without dicyandiamide and bulk g-C3N4 powders were prepared similarly but without the addition of h-BN.

2.2. Characterization

The powder X-ray diffraction (XRD) patterns were recorded using Bruker AXS D8 advance diffractometer operating with Cu-Ka source to investigate the crystal structure of the samples. The morphologies of resulting samples were characterized by a field emission scanning electron microscopy (SEM) (JSM-7001F, Japan) and transmission electron microscopy (TEM) (F20, USA). The X-ray photoelectron spectroscopy (XPS) (Thermo Fisher Scientific, UK) was carried out to analyze the surface electronic state. The specific surface area of these samples was characterized from the nitrogen absorption–desorption data and Brunauer–Emmett–Teller (BET) measurement (ASAP2020, Micromeritics, USA). UV–vis diffuse-reflectance spectra (UV–vis DRS) of as-synthesized samples were recorded in the range of 200–800 nm with a Varian Cary 300 spectrometer equipped with an integrating sphere. Photoluminescence (PL) spectroscopy was measured at the excitation wavelength of 350 nm on PerkinElmer LS-55 spectrofluorimeter at room temperature. Photocurrent measurements were performed on a CHI 660D electrochemical workstation (Shanghai Chenhua, China) using a three-electrode cell with the nanostructure materials on FTO as the working electrode, saturated Ag/AgCl and platinum electrode as the counter electrode and the reference electrode, respectively. The concentration of intermediate product H2O2 detected by the test paper (Merck, Germany). The electron spin resonce (ESR) signals were examined on a Bruker ER200-SRC spectrometer under visible light irradiation (λ > 420 nm).

2.3. Photocatalytic experiments

The photocatalytic measurements were carried out by using TC and RhB as target pollutants under visible light irradiation. A 300 W Xenon lamp (Beijing China Education Au-light, Co., Ltd.) with a 420 nm cutoff filter was used as the visible-light source. In a typical procedure,
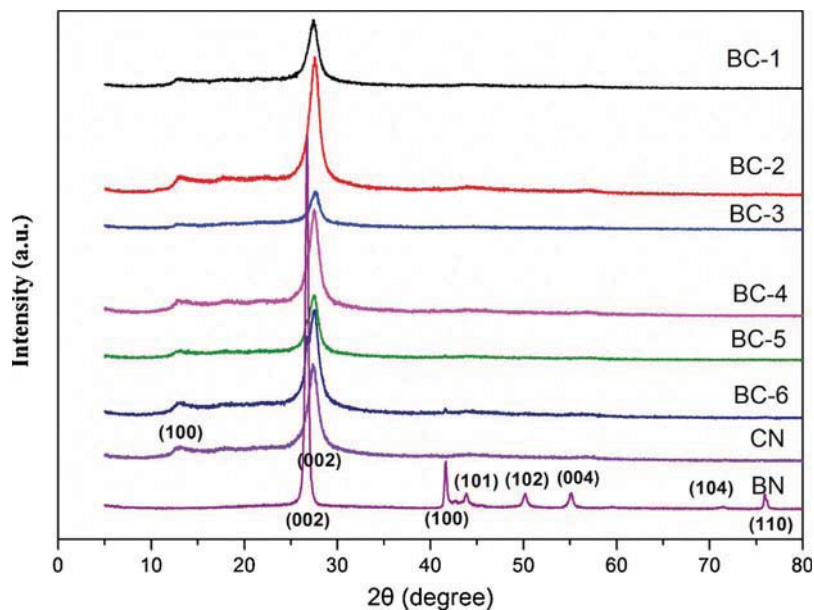
Fig. 1. XRD patterns of the prepared h-BN, g-C_3N_4 and h-BN/g-C_3N_4 composites.

100 mg photocatalysts were dispersed into 100 mL TC (10 mg L^{-1}) and 50 mg photocatalysts were dispersed into 100 mL RhB (20 mg L^{-1}). Before irradiation, the mixture was magnetically stirred for 60 min in the dark to establish an adsorption-desorption equilibrium. At a certain time interval of irradiation, 4 mL suspension was taken out and centrifuged to remove the photocatalyst particles. The concentrations of TC and RhB were analyzed with an UV–vis spectrophotometer (UV-2250, SHIMADZU Corporation, Japan).

3. Results and discussion

3.1. XRD analysis

The crystalline phases of the h-BN, g-C_3N_4 and h-BN/g-C_3N_4 hybrids with different amounts of h-BN were investigated by X-ray diffraction (XRD) (Fig. 1). Two characteristic peaks of g-C_3N_4 located at 13.1° for (100) reflection and 27.4° for (002) reflection could be observed [45]. The diffraction peaks at 2θ value of 26.8°, 41.6°, 43.9°, 50.1°, 55.2°, 71.4° and 75.9° were assigned to (002), (100), (101), (102), (004), (104) and (110) planes of hexagonal structure h-BN (JCPDS card no. 34-0421). However, there was no typical pattern of BN being observed in h-BN/g-C_3N_4 composites which might be due to the low BN content in the samples or high dispersion of h-BN. The similar results can also be found in other systems [46,47]. In addition, no any other characteristic peaks could be found, which showed that the high purity phases formed during the preparation process.

3.2. Chemical states analysis

The XPS was further employed to analyze the surface elemental composition and chemical state of the sample. Fig. 2a shows the XPS survey scan spectra of the as-prepared BC-3 composite, specifying the co-existence C, N, O, and B elements. A weak O 1s peak at 532.1 eV is accredited to the adsorbed H_2O or CO_2, which is a common phenomenon found in literatures [48]. High-resolution spectra of C1s (Fig. 2b) represents two peaks at the binding energies of 284.8 and 288.1 eV, respectively. The peak located at 284.8 eV is assigned to adventitious carbon species, and the peak at 288.1 eV is assigned to the tertiary carbon C-(N)3 in the g-C_3N_4 lattice [16,49]. In the N 1s XPS spectrums, the main N 1s peaks at 399.8 eV and 398.2 eV are due to the sp2-hybridized nitrogen (C=N−C) and N^{3-} in BN layer [47,50,51]. Fig. 2d shows the high-resolution XPS spectra of B 1s.The peak at 190.6 eV in B

1s spectra is assigned to B−N bonds [47]. Therefore, the experimental results revealed the successful preparation of chemical-coupling h-BN/g-C_3N_4 composites.

3.3. Morphology characterization

The morphologies of h-BN/g-C_3N_4 can be observed via SEM images presented in Fig. 3. For comparison, SEM images of pure g-C_3N_4 and h-BN were also included. From Fig. 3a, it can be seen that g-C_3N_4 samples exhibit an aggregated, slate-like, and different nanosizes crystals stacking layers with smooth structures, which is the typical structure characteristic of g-C_3N_4 synthesized by the polymerization method [44,48]. As shown in Fig. 3b, h-BN displays aggregated stacking small sheet-like morphology due to aggregation and gathering of the h-BN sheets. Indeed, the sheet-like morphology is confirmed by TEM observations of the h-BN (Fig. 4b). After introducing the h-BN, the h-BN/g-C_3N_4 composites samples appear some agglomeration nanosheets on the surface of g-C_3N_4, resulting in the formation of a heterostructure. Moreover, the surface of particles is less smooth than that of the pure g-C_3N_4, which may be due to the presence of h-BN nanosheets coating on the g-C_3N_4 layers. The morphology and microstructure of the synthesized samples were further analyzed by TEM observations. Fig. 4(a–c) displays the TEM images of CN, BN, and BC-3 nanocomposites, from which we find that CN shows typical layered platelet-like morphology with non-uniform in thickness and BN depicts typical sheet-like morphology.

3.4. Specific surface area and optical properties

The N_2 adsorption–desorption isotherms of as-prepared pure g-C_3N_4 and BC-3 samples were depicted in Fig. 5. The BET surface area of bare g-C_3N_4 and BC-3 was found to be 10.24 m^2 g^{-1} and 34.69 m^2 g^{-1}, respectively. It is known that the higher specific surface areas can provide abundant active reaction sites and facilitate more pollutant molecules being adsorbed on its surface [46,52]. Therefore, the h-BN/g-C_3N_4 composite is expected to possess a better photocatalytic activity than pure g-C_3N_4 for the degradation of organic pollutants. The average pore diameter of BC-3 was 22.44 nm, indicating the formation of mesoporous materials. The optical property of h-BN, g-C_3N_4, and h-BN/g-C_3N_4 composites was characterized using UV–vis diffuse reflectance spectroscopy. As depicted in Fig. 6a, pure g-C_3N_4 shows absorption wavelengths from the ultraviolet to the visible light region up to
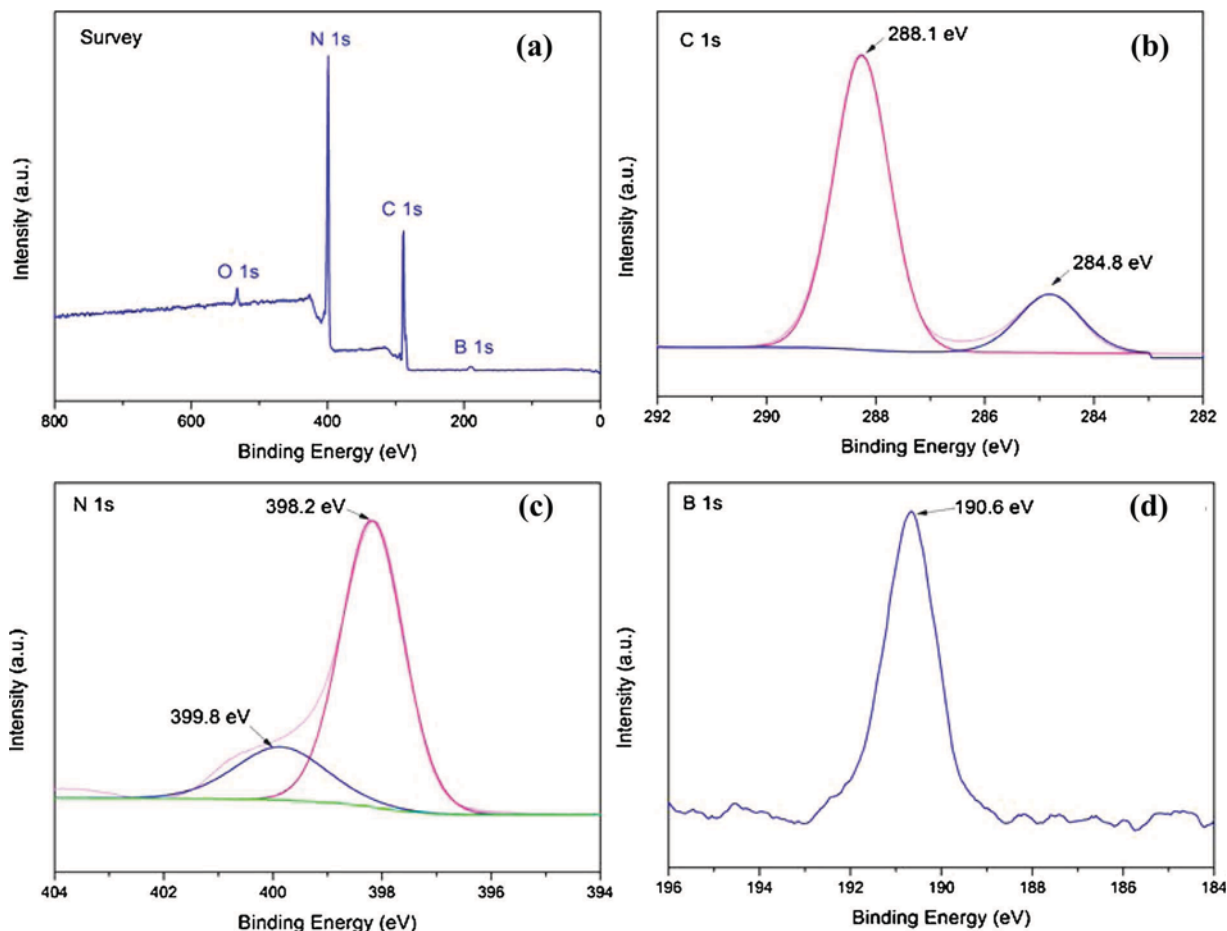
Fig. 2. XPS spectra of the BC-3 composite. (a) Survey of the sample; (b) C 1s; (c) N 1s and (d) B 1s.

460 nm, while no obvious absorption peak in the visible spectrum is detected for h-BN. It is well known that the optical absorption of a semiconductor is closely related to its electronic structure [48]. Therefore, the h-BN/g-C$_3$N$_4$ composites presented the hybrid absorption features of h-BN and g-C$_3$N$_4$. It can be seen that the absorption edge of h-BN/g-C$_3$N$_4$ composites exhibits somewhat blue-shift when compared to the pure g-C$_3$N$_4$. However, all of h-BN/g-C$_3$N$_4$ composites still reveal significant visible-light absorption suggesting that these composites can absorb visible-light and be applied for visible-light photocatalysis.

In general, the optical absorption band edge (E$_g$) of a semiconductor photocatalyst can be estimated according to the following formula:

$$\alpha h v = A(h v - E_g)^{n/2} \qquad (1)$$

where, α, h, v, A and E$_g$ represent the absorption coefficient, Planck constant, light frequency, a constant and band gap energy, respectively. The band gap energy for the g-C$_3$N$_4$ was determined from a plot of $(\alpha h v)^{1/2}$ vs. hv (n = 4 for indirect transition). Thus, the band gaps were estimated to be about 2.56 eV for g-C$_3$N$_4$, which were similar to the previous literatures [49].

In addition, the potentials of the VB and CB for h-BN and g-C$_3$N$_4$ can be calculated according to the following equations:

$$E_{CB} = X - E^e - \frac{1}{2}E_g \qquad (2)$$

$$E_{VB} = E_{CB} + E_g \qquad (3)$$

where E$_{VB}$ is the VB potential, E$_{CB}$ is the CB potential, X is the electronegativity of the semiconductor, E^e is the energy of free electrons on the hydrogen scale (about 4.5 eV), E$_g$ is the band gap energy of the semiconductor [50]. Based on the above formulas, the VB potential and CB potential of g-C$_3$N$_4$ were calculated to be 1.50 eV and −1.06 eV, respectively.

Photoluminescence (PL) spectra has been applied to reveal the charge carrier trapping, migration and recombination processes of the semiconductor photocatalysts since PL emission arises from the recombination of free carriers. It is well acknowledged that the higher PL intensity indicates the fast recombination of the charge carriers, resulting in lower photocatalytic activity [13,30]. As shown in Fig. 7, pure g-C$_3$N$_4$ sample has a main emission peak at about 453 nm duo to the band gap recombination of electron–hole pairs [49]. After the h-BN was introduced, the heterostructured sample showed lower PL emission intensity compared with that of pure g-C$_3$N$_4$, indicating that the recombination rate of photogenerated charge carriers become lower in BC-3 heterojunction. The much lower peak intensity implied that the cooperative effects between h-BN and g-C$_3$N$_4$ contributed to decreasing the recombination of electron-hole pairs effectively and enhancing the charge separation efficiency.

3.5. Photoelectrochemical properties

The effect of the prepared h-BN/g-C$_3$N$_4$ composites on the separation efficiency of electron-hole pairs was investigated by photoelectric current (PC) and electrochemical impedance spectroscopy (EIS) experiments. Fig. 8a depicts the transient photocurrent responses of pure g-C$_3$N$_4$ and BC-3. It is clearly shown that BC-3 hybrids displays higher photocurrent responses, which is about 3 times than that of pure g-C$_3$N$_4$. Because the photocurrent is mainly produced by the diffusion of photoexcited electrons; simultaneously, the photoexcited holes are transferred rapidly to surface of g-C$_3$N$_4$ due to the electrostatic
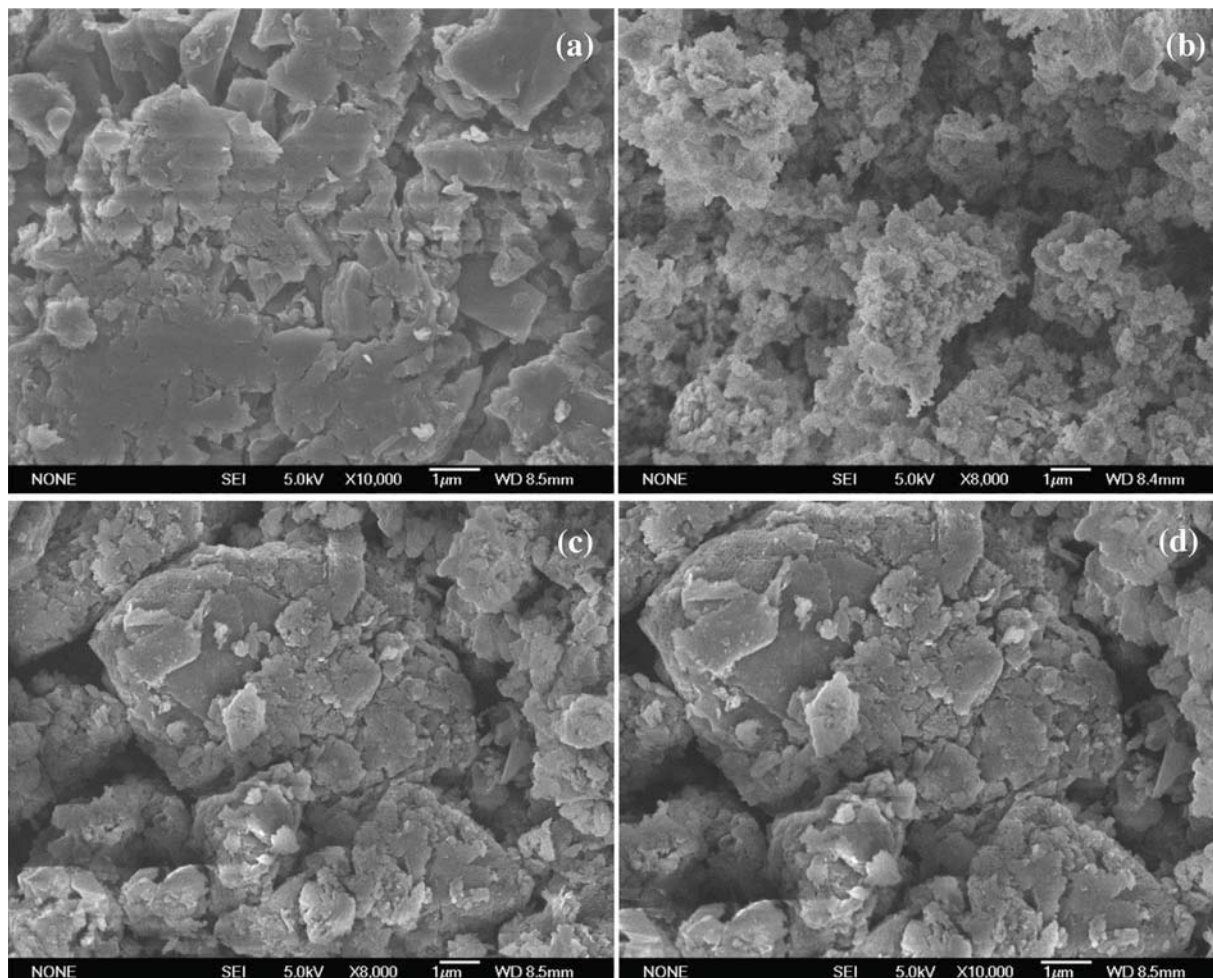
Fig. 3. SEM images of as-prepared samples (a) pure g-C$_3$N$_4$, (b) h-BN, (c, d) BC-3.

attraction between the holes and the negatively charged BN. Therefore, the enhanced photocurrent responses for the BC-3 means that the photoexcited carriers are separated effectively, and the photoexcited charge carriers have a long lifetime during the photocatalytic degradation reaction. The same result was obtained using an electrochemical impedance spectroscopy experiment. Fig. 8b depicts the EIS changes of g-C$_3$N$_4$, h-BN, and BC-3 electrodes. In general, the smaller arc in an EIS Nyquist plot indicates a smaller charge-transfer resistance on the electrode surface [30]. The data in Fig. 8b displays that relative arc sizes for the three electrodes are BC-3 < CN < BN. This confirms that the BC-3 composite has the highest efficiency in charge separation.

The PC and EIS results indicated that the combination with h-BN could greatly inhibit the recombination of electron-hole pairs and efficiently facilitate the separation of photogenerated charges at the interface between BN and g-C$_3$N$_4$. The results of PC and EIS were consistent with the PL analysis, which further validats that the introduction of h-BN is an effective way to improve photocatalytic performance.

3.6. Photocatalytic activity

The photocatalytic activities of the h-BN/g-C$_3$N$_4$ samples were evaluated by photocatalytic degradation of TC and RhB solution under

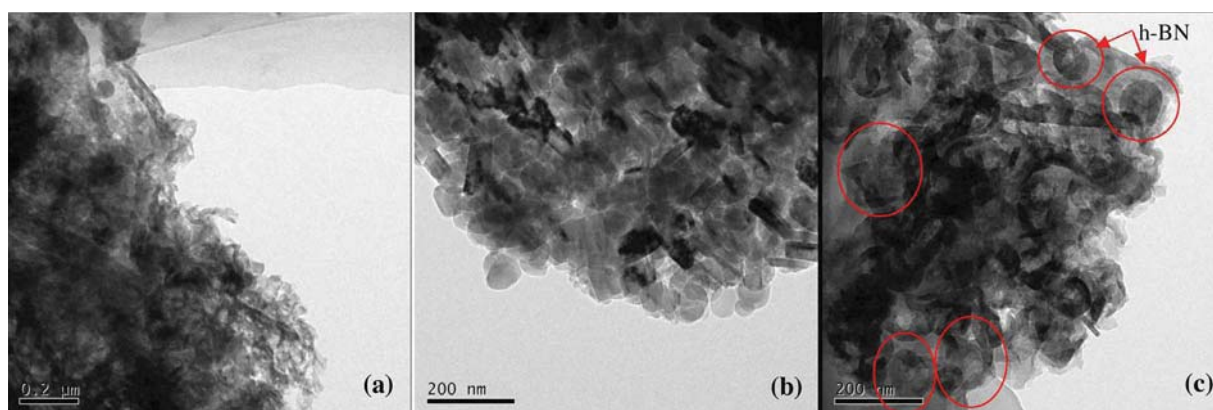Fig. 4. TEM micrographs of (a) pure g-C$_3$N$_4$, (b) h-BN, and (c) BC-3.
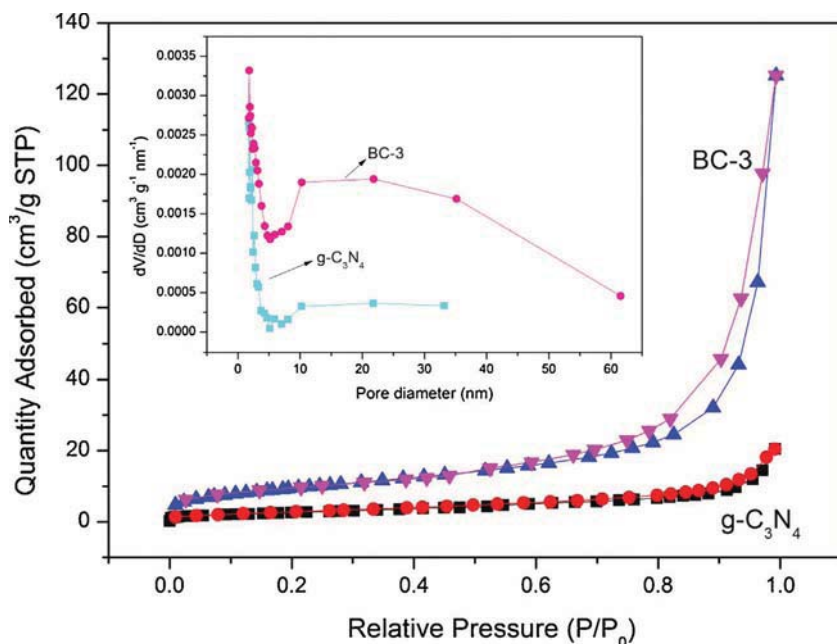
Fig. 5. N$_2$ adsorption–desorption isotherms and the corresponding pore size distribution (inset) of as-prepared pure g-C$_3$N$_4$ and BC-3 samples.

visible light. For comparison, the photocatalytic properties of h-BN and g-C$_3$N$_4$ were also tested under identical experimental conditions. Before irradiation, the solution including pollutant and photocatalysts was magnetically stirred for 60 min in the dark to establish an adsorption-desorption equilibrium. As depicted in Fig. 9a, the photocatalytic performance is significantly enhanced in the presence of the h-BN/g-C$_3$N$_4$ composites. To be specific, the photocatalytic efficiency of pure h-BN and g-C$_3$N$_4$ for TC were 4.4% and 52.8%, respectively. For the h-BN/g-C$_3$N$_4$ photocatalysts, it was obvious that the photocatalytic activity enhanced significantly with the increased amount of h-BN. When the h-BN amount was 2 mg in h-BN/g-C$_3$N$_4$ photocatalysts, BC-3 performed best and 79.7% TC was photodegraded in 60 min. The enhanced photocatalytic activity might be caused by that the BN nanosheet modification could endow higher separation efficiency of photogenerated electron–hole pairs for h-BN/g-C$_3$N$_4$ composites [35,41]. However, the photocatalytic activity of the photocatalyst decreased gradually when the amount of h-BN further increased. This was ascribed to that too much content of h-BN coated on the surface of g-C$_3$N$_4$ would shield the g-C$_3$N$_4$ from absorbing visible light, although the modification of h-BN nanosheet favored the charge separation. The lower light harvesting would reduce the generation of electron–hole pairs [46]. Therefore, too many h-BN nanosheet could lead to the decrease of photocatalytic
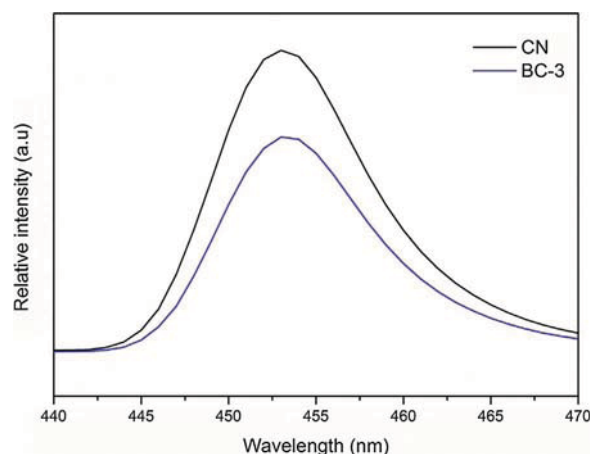

Fig. 7. Photoluminescence spectra of the obtained pure g-C$_3$N$_4$ and BC-3.

activity. Similar to TC degradation, the photocatalytic performance is significantly enhanced with 99.5% of RhB photodegraded in 40 min for BC-3 sample while the photocatalytic efficiency of pure h-BN and g-C$_3$N$_4$ for RhB are 34.7% and 54.1% as shown in Fig. 9c, respectively.
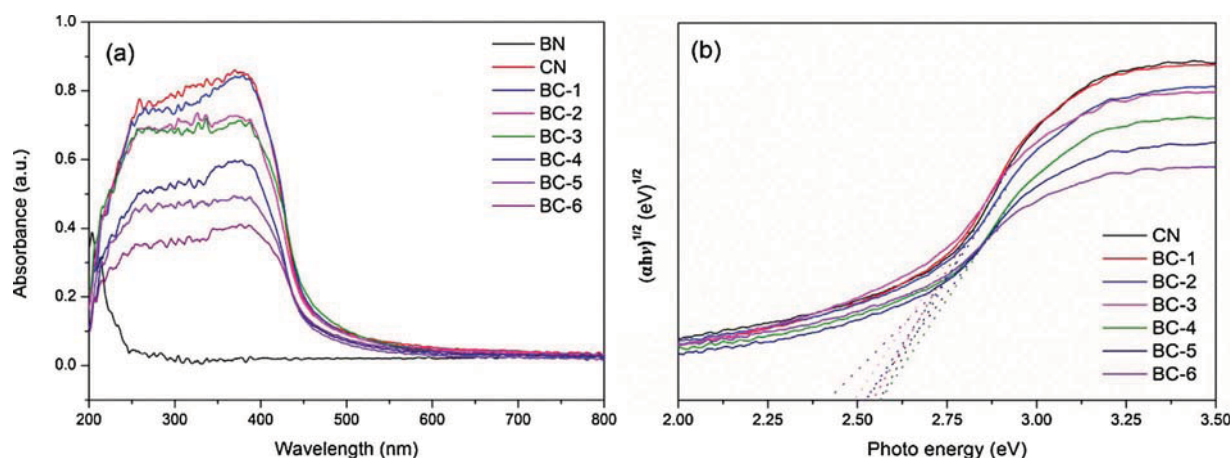

Fig. 6. (a) UV–vis spectrum and (b) plot of (αhν)$^{1/2}$ vs. photon energy (hν) of h-BN/g-C$_3$N$_4$ composites.
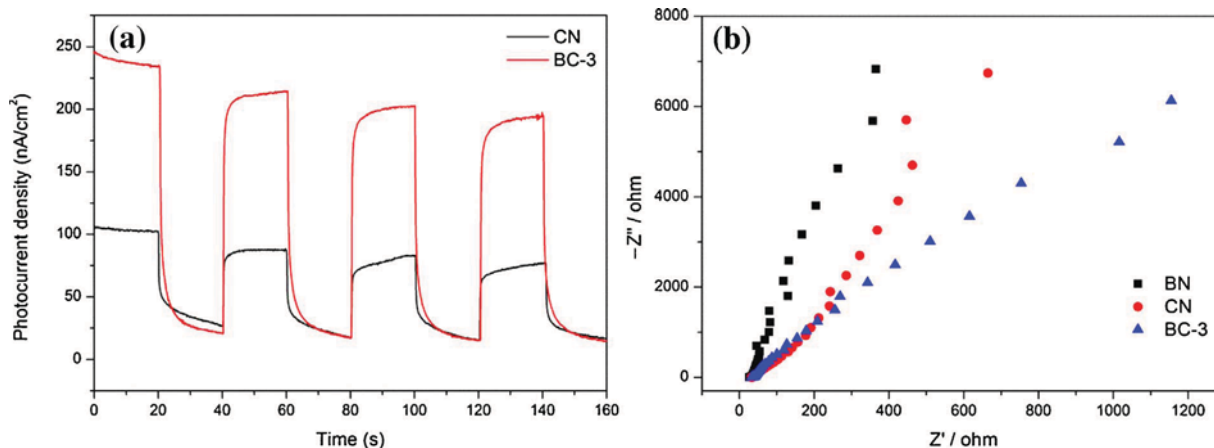
Fig. 8. Transient photocurrent responses (a) and Electrochemical impedance spectroscopy (EIS) changes (b) of the as-prepared samples.
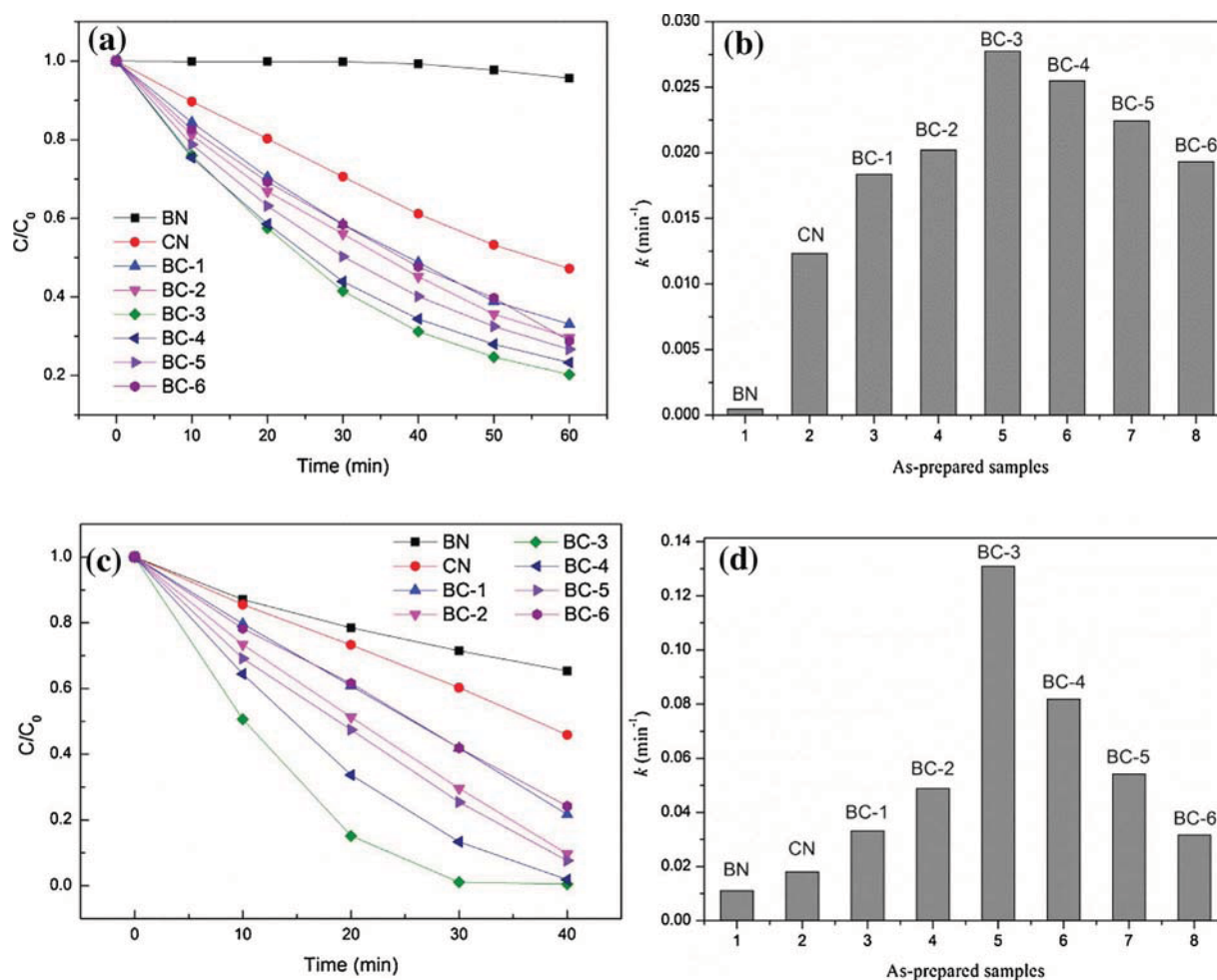

Fig. 9. (a) The photocatalytic activities of as-prepared samples for TC degradation under visible-light ($\lambda > 420$ nm); (b) The apparent rate constants for TC degradation; (c) The photocatalytic activities of as-prepared samples for RhB degradation under visible-light ($\lambda > 420$ nm); (d) The apparent rate constants for RhB degradation.

Considering that h-BN showed no visible light absorption (Fig. 6a), the observed activity may caused by the dye-sensitization effect, since the colored RhB dye usually absorb visible-light [44,46].

The kinetic behaviors of h-BN/g-C$_3$N$_4$ samples for photodegradation of TC and RhB were investigated. All of them fit well with the pseudo-first-order kinetics model:

$$- \ln(C/C_0) = kt \qquad (4)$$

where C$_0$ (mg L^{-1}) is the initial concentration, C (mg L^{-1}) is the remaining concentration at irradiation time of t, and k (min^{-1}) is the apparent first-order rate constant. The k values of different samples were shown in Fig. 9b and d, it can be found that the photocatalytic activities of the hybrids for TC and RhB degradation both exhibit a rise first followed by a decline with the increasing of h-BN content. BC-3 exhibited the highest rate constant, which is attributed to the larger surface area and the enhanced separation efficiency of photogenerated electron–hole pairs among the catalysts. The k value for TC degradation over BC-3 (0.02775 min^{-1}) sample was about 60.3 times higher than
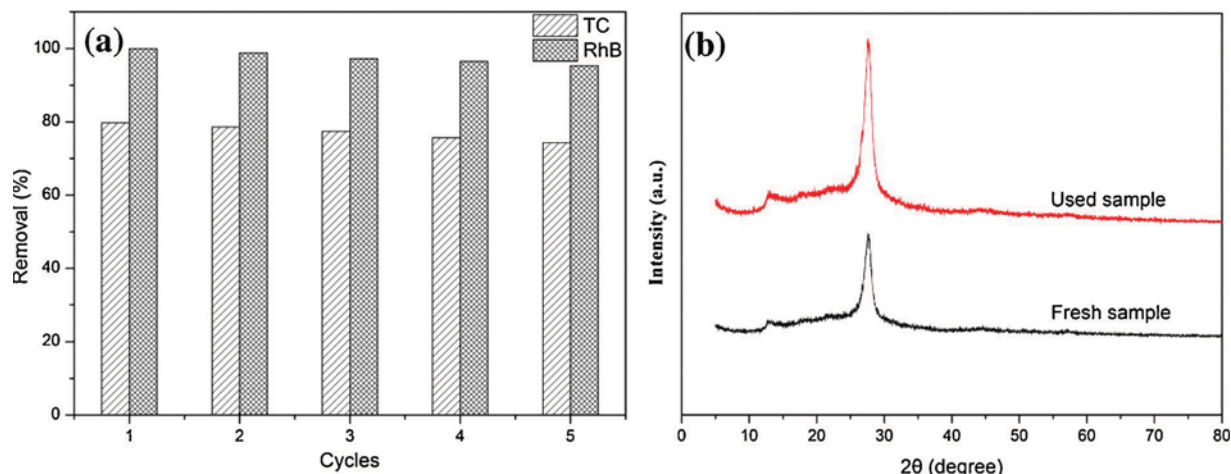
Fig. 10. (a) The repeated photocatalytic experiments of BC-3 photocatalyst for degradation of TC and RhB under visible light irradiation; (b) The XRD pattern of the BC-3 sample after 5th run cycle photocatalytic experiments.

that of h-BN (0.00046 min^{-1}), and 2.3 times than that of pure g-C$_3$N$_4$ (0.01233 min^{-1}). Similarly, the k value for RhB degradation over BC-3 (0.13091 min^{-1}) sample was about 11.8 times higher than that of h-BN (0.01111 min^{-1}), and 7.3 times than that of pure g-C$_3$N$_4$ (0.01805 min^{-1}). Although the high photoactivity of the h-BN/g-C$_3$N$_4$ composites has been verified, their stability with regard to practical applications was not clear. To test the stability of the h-BN/g-C$_3$N$_4$ composites, the BC-3 sample was collected after photodegradation experiment of TC for the recycle experiments. As shown in Fig. 10a, it can be observed that the photocatalytic activity of the BC-3 sample has no apparent deactivation even after five successive recycles for the degradation of TC (74.3%) and RhB (95.3%) under visible light irradiation, which indicates that our photocatalyst possess high stability for its practical application. Moreover, the BC-3 samples of before and after 5th run cycle were characterized by XRD analysis (Fig. 10b). It could be found that the phase and structure of the recycled BC-3 composite had almost no obvious discrepancy compared with the unirradiated one. This can be further confirmed by the chemical constituent of recycled BC-3 after TC degradation analyzed by XPS. The full–scan spectrum and high resolution spectra (Fig. S1) also presented a very similar result to the fresh BC-3. The results revealed that the sample is stable even after the 5th run cycle photocatalytic degradation processes.

3.7. Comparison with other photocatalysts

The comparisons of photocatalytic activities of the h-BN/g-C$_3$N$_4$ composite with various related g-C$_3$N$_4$ based metal-free photocatalysts previously reported for the photocatalytic degradation of TC and RhB were listed in Table 1. As can be seen, the TC removal and rate constant of BC-3 composite was 79.7% and 0.02775 min^{-1} within 60 min, which is preponderant compared with other carbonaceous materials modified g-C$_3$N$_4$ based metal-free photocatalysts such as N-CNT/mpg-C$_3$N$_4$ [53], CQDs/g-C$_3$N$_4$ [54] and GQDs/mpg-C$_3$N$_4$ [55]. Furthermore, BC-3 exhibits superior RhB photocatalytic degradation performance compared with GO/g-C$_3$N$_4$ [33], N-CNT/mpg-C$_3$N$_4$ [53], OMC/g-C$_3$N$_4$ [56], C$_{60}$/C$_3$N$_4$ [57], CCN/g-C$_3$N$_4$ [58], g-C$_3$N$_4$/S-g-C$_3$N$_4$ [59], g-C$_3$N$_4$/g-C$_3$N$_4$ [60,61], CQDs/g-C$_3$N$_4$ [54], GQDs/mpg-C$_3$N$_4$ [55] and S,N-GQDs/g-C$_3$N$_4$ [62]. This verifies that h-BN/g-C$_3$N$_4$ composites have great potentials for both TC and RhB removal from contaminated water.

3.8. Photocatalytic mechanism

It is generally recognized that photo-induced reactive species including trapped holes (h$^+$), hydroxyl radicals (·OH) and superoxide radicals (·O$_2^-$) are expected to be involved in the photocatalytic

process. In order to explore the predominant active species generated in the reaction system, 1,4-benzoquinone (BQ), triethanolamine (TEA) and isopropanol (IPA) were employed as the scavengers of superoxide radical (·O$_2^-$) [25]. hole (h$^+$) [49] and hydroxyl radical (·OH), [30] respectively. The corresponding active species will be efficiently quenched in the pollutant photodegradation after being trapped, and the degradation efficiency thus becomes lower. As shown in Fig. 11, the radical trapping results of CN and BC-3 exhibit a similar trend. As for BC-3, the photocatalytic efficiency of TC decreased from 79.7% to 24.6% when TEA was added, indicating the h$^+$ is the predominant active species. Similarly, a significant loss of the degradation rate could be found with the addition of BQ, verifying the ·O$_2^-$ pathway also possess a crucial role in the photocatalytic process. However, ignorable inhibition was shown by IPA, indicating that the ·OH does not contribute to the degradation of TC. The similar result could be found in the photodegradation of RhB solution for BC-3 (Fig. 11d). Therefore, it was indicated that h$^+$ and ·O$_2^-$ are the dominant active species generated in the photocatalytic process, which should be responsible for the highly enhanced photocatalytic performance for TC and RhB degradation. As described by the photocurrent and EIS analysis, the presence of h-BN nanosheets in the h-BN/g-C$_3$N$_4$ composites could effectively inhibit the electron-hole pair recombination, which might cause more radical species with strong oxidation capability.

In order to further confirm the presence of ·OH and ·O$_2^-$ radicals in the g-C$_3$N$_4$ and BC-3 photocatalytic reaction systems under visible light, the electron spin resonance (ESR) spin-trap technique was carried out. DMPO (5,5-dimethyl-1-pyrroline N-oxide), a nitrone spin trapping reagent, was utilized to capture the superoxide (·O$_2^-$) and hydroxyl radicals (·OH) [63,64]. All the experiments were conducted under dark condition and visible light irradiation of 4 min, 8 min and 12 min. As depicted in Fig. 12a and c, six characteristic peaks of DMPO-·O$_2^-$ are observed in the methanol dispersion of g-C$_3$N$_4$ and BC-3 under visible light irradiation, which implying the ·O$_2^-$ radical species are produced via single-electron reduction process [46]. It is reasonable for the ·O$_2^-$ production in BC-3 system as the photogenerated electrons of g-C$_3$N$_4$ have the ability to trap molecular oxygen to generate ·O$_2^-$ (Fig. 12a). This could be explained by that the CB potentials (-1.06 eV vs NHE) of g-C$_3$N$_4$ are more negative than the reduction potential (-0.33 eV vs NHE) of O$_2$/·O$_2^-$. Interestingly, the typical characteristic peaks of DMPO-·OH adducts (Fig. 12b and d) were also observed, indicating that the ·OH radicals are also produced in both g-C$_3$N$_4$ and BC-3 reaction systems. However, the results obtained from active species trapping experiments illustrated that ·OH radicals had little effect on the TC and RhB degradation for both g-C$_3$N$_4$ and BC-3. It might be caused by the fact that the observed DMPO-·OH signal in Fig. 12b and d

Table 1
Comparison with other g-C_3N_4 based metal-free photocatalysts in the literature.

Photocatalyst	Pollutant	Concentration (mg L^{-1})	Dosage (g L^{-1})	Time (min)	Removal (%)	Rate (min^{-1})	Light source	Reference
N-CNT/mpg-C_3N_4	TC	20	1.0	240	67.1	–	300 W XL ($\lambda \geq 400$ nm)	[53]
CQDs/g-C_3N_4	TC	10	0.5	240	78.6	0.00642	250 W XL ($\lambda \geq 420$ nm)	[54]
GQDs/mpg-C_3N_4	TC	20	1.0	120	≈ 65	–	300 W XL ($\lambda > 400$ nm)	[55]
h-BN/g-C_3N_4	**TC**	**10**	**1.0**	**60**	**79.7**	**0.02775**	**300 W XL ($\lambda \geq 420$ nm)**	**In this study**
GO/g-C_3N_4	RhB	10	–	150	94.2	≈ 0.0152	150 W XL ($\lambda \geq 400$ nm)	[33]
N-CNT/mpg-C_3N_4	RhB	10	0.5	60	95	–	300 W XL ($\lambda \geq 400$ nm)	[53]
OMC/g-C_3N_4	RhB	5	0.5	60	–	0.0534	300 W XL ($\lambda \geq 400$ nm)	[56]
C_{60}/C_3N_4	RhB	4.79	0.6	60	97	0.05818	500 W XL ($\lambda \geq 420$ nm)	[57]
CCN/g-C_3N_4	RhB	10	0.15	150	93.3	0.01767	300 W XL ($\lambda \geq 400$ nm)	[58]
g-C_3N_4/S-g-C_3N_4	RhB	10	0.25	120	92	0.0228	250 W SL ($400 \leq \lambda \leq 800$ nm)	[59]
g-C_3N_4/g-C_3N_4	RhB	5	1.0	60	90	–	300 W XL ($\lambda \geq 400$ nm)	[60]
g-C_3N_4/g-C_3N_4	RhB	10	1.0	12	97 (+ adsorption)	–	300 W XL ($\lambda \geq 400$ nm)	[61]
CQDs/g-C_3N_4	RhB	10	0.5	210	95.2	0.01438	250 W XL ($\lambda \geq 420$ nm)	[54]
GQDs/mpg-C_3N_4	RhB	10	0.5	120	97	–	300 W XL ($\lambda > 400$ nm)	[55]
S,N-GQDs/g-C_3N_4	RhB	5	0.5	90	96	0.0388	500 W XL ($\lambda \geq 420$ nm)	[62]
h-BN/g-C_3N_4	**RhB**	**20**	**0.5**	**40**	**99.5**	**0.13091**	**300 W XL ($\lambda \geq 420$ nm)**	**In this study**

GO: graphene oxide; N-CNT: Nitrogen-doped carbon nanotubes; mpg-C_3N_4: mesoporous graphitic carbon nitride; OMC: Ordered mesoporous carbon; C_{60}: Fullerene; CCN: Crystalline carbon nitride; S-g-C_3N_4: S doped g-C_3N_4; CQDs: Carbon quantum dots; XL: Xenon lamp; SL: High-pressure sodium lamp; S,N-GQDs: S,N co-doped graphene quantum dots.

is attributed to the further reduction of $\cdot O_2^-$ via $\cdot O_2^- \rightarrow H_2O_2 \rightarrow \cdot OH$ [63,65], as the VB potential (1.50 eV vs NHE) of g-C_3N_4 is not positive enough to oxidize the water or surface hydroxyl group to form $\cdot OH$. Recently, Liu et al. confirmed the presence of H_2O_2 diffusion layer on C_3N_4 during photocatalysis by a Pt tip [66]. Furthermore, the CB level of g-C_3N_4 (-1.06 eV vs. NHE) is more negative than that ($+0.69$ V vs. NHE) of reaction: $e_{CB}^- + O_2 + 2H^+ \rightarrow H_2O_2$ [63,65,67]. Furthermore, the intermediate product H_2O_2 has be detected by the test paper which indicated that the concentration was less than 0.5 mg/L (Fig. S2).Thus,

the electrons would react with resolved O_2 and H^+ to produce H_2O_2 which could be further reduced to $\cdot OH$ radicals as reaction: $e_{CB}^- + H_2O_2 \rightarrow \cdot OH + OH^-$ [67]. Therefore, according to the above results of the radical trapping experiments and this ESR analysis, the overall reaction mechanism and process of TC and RhB degradation over h-BN/g-C_3N_4 under visible light irradiation were schematized in Fig. 13. When h-BN/g-C_3N_4 composite is irradiated by visible light, the g-C_3N_4 can be easily excited and produce the photogenerated electrons and holes in the CB and VB, respectively. The holes photoexcited by g-
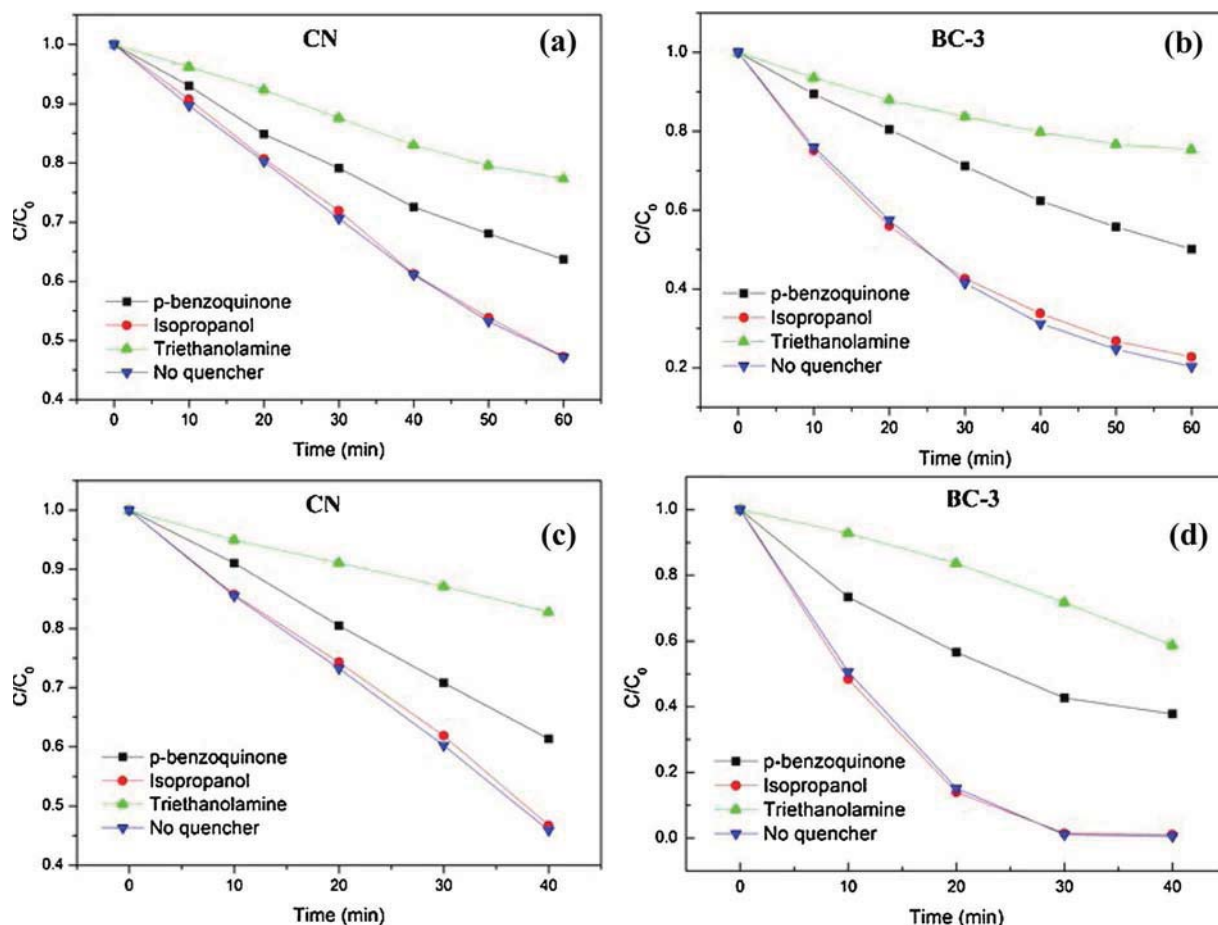

Fig. 11. The species trapping experiments for degradation of TC and RhB over CN and BC-3 photocatalysts under visible light irradiation, (a, b) TC; (c, d) RhB.
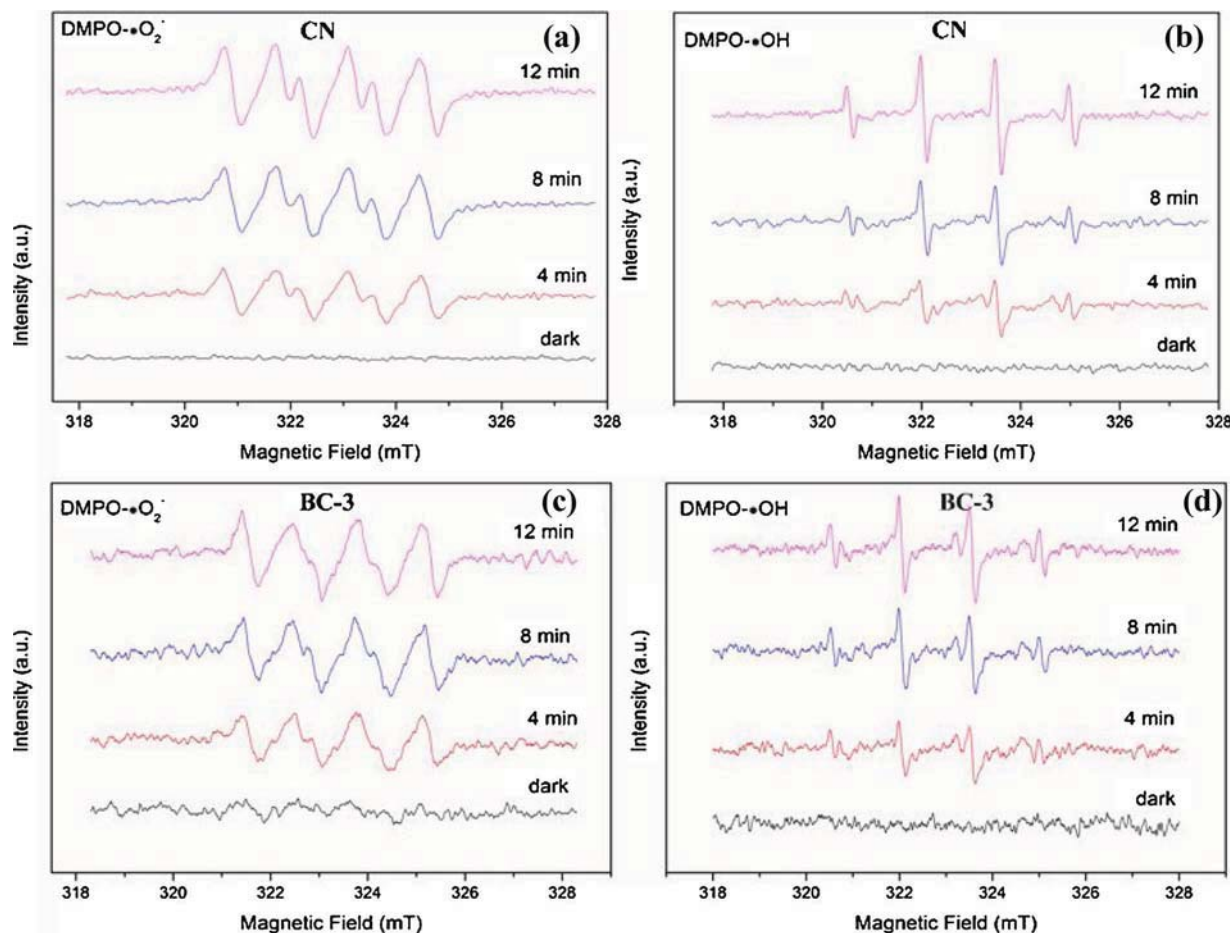
Fig. 12. DMPO spin-trapping ESR spectra with CN and BC-3 sample in methanol dispersion (for DMPO-$\cdot O_2^-$) and in aqueous dispersion (for DMPO-$\cdot OH$) under visible light irradiation.
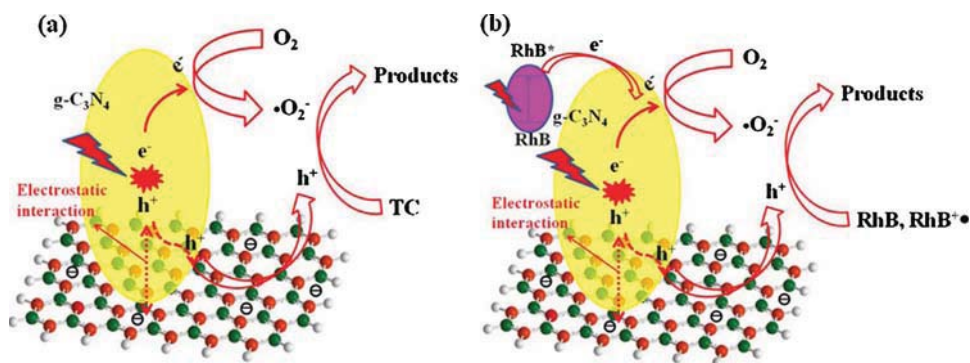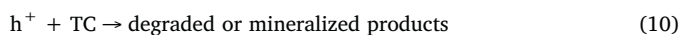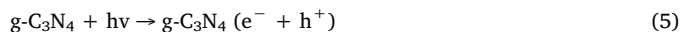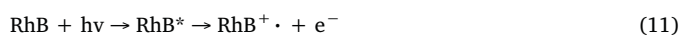

Fig. 13. Schematic of the separation and transfer of photogenerated charges in the h-BN/g-C_3N_4 composites combined with the possible reaction mechanism of the photocatalytic procedure, (a) TC degradation; (b) RhB degradation.
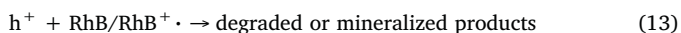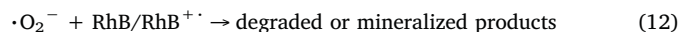
C_3N_4 are transferred rapidly to its surface due to the electrostatic attraction between the holes and the negatively charged BN, and then participate in photocatalytic reaction [35,41]. More importantly, it is favorable for efficient separation of photoexcited electron-hole pairs and prolonging electrons lifetime. At the same time, the photoexcited electrons will be captured by the dissolved O_2 to generate $\cdot O_2^-$, which directly oxidize the TC molecules in the aqueous solution. While for RhB photodegradation, the RhB molecules adsorbed on the surface of h-BN/g-C_3N_4 composite could be changed into its excited state (RhB*) and inject the electrons into the CB of g-C_3N_4. As depicted in Fig. 13b, both the electrons from the excited RhB molecules and g-C_3N_4 could reduce the adsorbed O_2 to $\cdot O_2^-$ which directly participate in the oxidation reaction. Subsequently, the holes in the VB of g-C_3N_4 would transfer to its surface and then oxidize the RhB molecules in the aqueous solution. However, when no h-BN was modified on the g-C_3N_4, the

generated charge pairs cannot be effective separated and large portion of charge carriers would recombine.

$$g\text{-}C_3N_4 + hv \rightarrow g\text{-}C_3N_4\ (e^- + h^+) \tag{5}$$

$$e^- + O_2 \rightarrow \cdot O_2^- \tag{6}$$

$$\cdot O_2^- + 2H^+ + e^- \rightarrow H_2O_2 \tag{7}$$

$$H_2O_2 + e^- \rightarrow \cdot OH + OH^- \tag{8}$$

$$\cdot O_2^- + TC \rightarrow \text{degraded or mineralized products} \tag{9}$$

$$h^+ + TC \rightarrow \text{degraded or mineralized products} \tag{10}$$

While for RhB degradation, the followed additional reaction was happened.

$$RhB + hv \rightarrow RhB^* \rightarrow RhB^+ \cdot + e^- \tag{11}$$

$$\cdot O_2{}^- + RhB/RhB^{+\cdot} \rightarrow degraded\ or\ mineralized\ products \qquad (12)$$

$$h^+ + RhB/RhB^{+\cdot} \rightarrow degraded\ or\ mineralized\ products \qquad (13)$$

It is generally acknowledged that the high surface area, good light absorption capability, and high separation efficiency of electron–hole pairs are beneficial for the performance of a photocatalyst. However, the DRS result indicates that the addition of h-BN slightly decreases the photoabsorption performance of g-C_3N_4. Therefore, the high photocatalytic activity of h-BN/g-C_3N_4 composites could be caused by the larger surface area and higher separation efficiency of electron–hole pairs. PL, PC, and EIS were employed to check the separation efficiency of electron–hole pairs under visible light irradiation. As expected, the PL, PC, and EIS experiments show that the introduction of h-BN to g-C_3N_4 greatly promotes the separation efficiency of electron–hole pairs [46,51].

4. Conclusions

In summary, h-BN/g-C_3N_4 metal-free heterojunction was prepared by a facile in situ growing method. The h-BN was well-dispersed on the g-C_3N_4 materials and tight contact interface has been constructed. Compared to pristine g-C_3N_4, enhanced photocatalytic oxidation of TC and RhB under visible light was achieved. When the h-BN amount was 0.48 wt.% in h-BN/g-C_3N_4 photocatalysts, BC-3 performed best. 79.7% TC and 99.5% RhB was photodegraded under visible light irradiation for 60 min and 40 min, respectively. The photocatalytic degradation of TC and RhB over the samples obeyed pseudo-first-order kinetics, and the photodegradation rate over BC-3 sample for TC degradation is 0.02775 min^{-1}, about 60.3 and 2.3 times higher than that of h-BN and pure g-C_3N_4. Meanwhile, the photodegradation rate over BC-3 sample for RhB degradation is about 11.8 and 7.3 times higher than that of h-BN and pure g-C_3N_4. This enhanced photocatalytic capability of h-BN/g-C_3N_4 is mainly due to the larger surface area and the facilitated separation of photogenerated carriers owing to the heterojunction built between h-BN and g-C_3N_4. The photo-degradation is dominant by the $\cdot O_2{}^-$ and hole oxidation process while $\cdot OH$ radicals could be neglected.

Acknowledgements

Appendix A. Supplementary data

Supplementary data associated with this article can be found, in the online version, at http://dx.doi.org/10.1016/j.apcatb.2017.09.059.

References

[1] Z. Wu, X. Yuan, J. Zhang, H. Wang, L. Jiang, G. Zeng, ChemCatChem 9 (2017) 41–64.
[2] E. Neyens, J. Baeyens, J. Hazard. Mater. 98 (2003) 33–50.
[3] J. Jeong, J. Yoon, Water Res. 39 (2005) 2893–2900.
[4] B. Ai, X. Duan, H. Sun, X. Qiu, S. Wang, Catal. Today 258 (2015) 668–675.
[5] S. Fang, K. Lv, Q. Li, H. Ye, D. Du, M. Li, Appl. Surf. Sci. 358 (2015) 336–342.
[6] L. Jiang, X. Yuan, Y. Pan, J. Liang, G. Zeng, Z. Wu, H. Wang, Appl. Catal. B: Environ. 217 (2017) 388–406.
[7] L. Jiang, X. Yuan, G. Zeng, X. Chen, Z. Wu, J. Liang, J. Zhang, H. Wang, H. Wang, ACS Sustain. Chem. Eng. 5 (2017) 5831–5841.
[8] X. Yuan, L. Jiang, X. Chen, L. Leng, W. Hou, Z. Wu, T. Xiong, J. Liang, G. Zeng, Environ. Sci. Nano (2017), http://dx.doi.org/10.1039/C7EN00713B.
[9] K. Rajeshwar, M.E. Osugi, W. Chanmanee, C.R. Chenthamarakshan, M.V.B. Zanoni, P. Kajitvichyanukul, R. Krishnan-Ayer, J. Photochem. Photobiol. C: Photochem. Rev. 9 (2008) 171–192.
[10] M.M. Khin, A.S. Nair, V.J. Babu, R. Murugan, S. Ramakrishna, Energy Environ. Sci. 5 (2012) 8075.
[11] H.S. Jung, Y.J. Hong, Y. Li, J. Cho, Y.-J. Kim, G.-C. Yi, ACS Nano 2 (2008) 637–642.
[12] J. Su, P. Geng, X. Li, Q. Zhao, X. Quan, G. Chen, Nanoscale 7 (2015) 16282–16289.
[13] N. Liang, J. Zai, M. Xu, Q. Zhu, X. Wei, X. Qian, J. Mater. Chem. A 2 (2014) 4208.
[14] C. Xing, Z. Wu, D. Jiang, M. Chen, J. Colloid Interface Sci. 433 (2014) 9–15.
[15] W.J. Ong, L.L. Tan, Y.H. Ng, S.T. Yong, S.P. Chai, Chem. Rev. 116 (2016) 7159–7329.
[16] F. Dong, Z. Zhao, T. Xiong, Z. Ni, W. Zhang, Y. Sun, W.K. Ho, ACS Appl. Mater. Interfaces 5 (2013) 11392–11401.
[17] Y. Liu, X. Yuan, H. Wang, X. Chen, S. Gu, Q. Jiang, Z. Wu, L. Jiang, Y. Wu, G. Zeng, Catal. Commun. 70 (2015) 17–20.
[18] D. Lu, H. Wang, X. Zhao, K.K. Kondamareddy, J. Ding, C. Li, P. Fang, ACS Sustain. Chem. Eng. 5 (2017) 1436–1445.
[19] X.P. Xiao, J.H. Wei, Y. Yang, R. Xiong, C.X. Pan, J. Shi, ACS Sustain. Chem. Eng. 4 (2016) 3017–3023.
[20] J. Zhu, P. Xiao, H. Li, S.A.C. Carabineiro, ACS Appl. Mater. Interfaces 6 (2014) 16449–16465.
[21] X. Wang, K. Maeda, A. Thomas, K. Takanabe, G. Xin, J.M. Carlsson, K. Domen, M. Antonietti, Nat. Mater. 8 (2008) 76–80.
[22] Z. Huang, Q. Sun, K. Lv, Z. Zhang, M. Li, B. Li, Appl. Catal. B: Environ. 164 (2015) 420–427.
[23] S. Fang, Y. Xia, K. Lv, Q. Li, J. Sun, M. Li, Appl. Catal. B: Environ. 185 (2016) 225–232.
[24] X. Li, J. Zhang, X. Chen, A. Fischer, A. Thomas, M. Antonietti, X. Wang, Chem. Mater. 23 (2011) 4344–4348.
[25] Y. Huang, W. Fan, B. Long, H. Li, F. Zhao, Z. Liu, Y. Tong, H. Ji, Appl. Catal. B: Environ. 185 (2016) 68–76.
[26] J. Li, M. Han, Y. Guo, F. Wang, C. Sun, Chem. Eng. J. 298 (2016) 300–308.
[27] M. Xiong, L. Chen, Q. Yuan, J. He, S.L. Luo, C.T. Au, S.F. Yin, Dalton Trans. 43 (2014) 8331–8337.
[28] P. Qiu, J. Yao, H. Chen, F. Jiang, X. Xie, J. Hazard. Mater. 317 (2016) 158–168.
[29] Y. Guo, J. Li, Z. Gao, X. Zhu, Y. Liu, Z. Wei, W. Zhao, C. Sun, Appl. Catal. B: Environ. 192 (2016) 57–71.
[30] Y. He, L. Zhang, B. Teng, M. Fan, Environ. Sci. Technol. 49 (2015) 649–656.
[31] Y. Xu, H. Xu, L. Wang, J. Yan, H. Li, Y. Song, L. Huang, G. Cai, Dalton Trans. 42 (2013) 7604.
[32] Y. Chen, J. Li, Z. Hong, B. Shen, B. Lin, B. Gao, Phys. Chem. Chem. Phys. 16 (2014) 8106.
[33] G. Liao, S. Chen, X. Quan, H. Yu, H. Zhao, J. Mater. Chem. 22 (2012) 2721–2726.
[34] L. Jiang, X. Yuan, J. Liang, J. Zhang, H. Wang, G. Zeng, J. Power Sources 331 (2016) 408–425.
[35] S. Meng, X. Ye, X. Ning, M. Xie, X. Fu, S. Chen, Appl. Catal. B: Environ. 182 (2016) 356–368.
[36] D. Golberg, Y. Bando, Y. Huang, T. Terao, M. Mitome, C. Tang, C. Zhi, ACS Nano 4 (2010) 2979–2993.
[37] D. Liu, W. Cui, J. Lin, Y. Xue, Y. Huang, J. Li, J. Zhang, Z. Liu, C. Tang, Catal. Commun. 57 (2014) 9–13.
[38] V. Štengl, J. Henych, M. Slušná, J. Nanomater. 2016 (2016) 1–12.
[39] R. Zhang, J. Wang, P. Han, J. Alloys Compd. 637 (2015) 483–488.
[40] C. Tang, J. Li, Y. Bando, C. Zhi, D. Golberg, Chem. Asian J. 5 (2010) 1220–1224.
[41] X. Fu, Y. Hu, Y. Yang, W. Liu, S. Chen, J. Hazard. Mater. 244–245 (2013) 102–110.
[42] X. Fu, Y. Hu, T. Zhang, S. Chen, Appl. Surf. Sci. 280 (2013) 828–835.
[43] M.R. Hoffmann, S.T. Martin, W. Choi, D.W. Bahnemann, Chem. Rev. 95 (1995) 69–96.
[44] H. Wang, X. Yuan, Y. Wu, G. Zeng, X. Chen, L. Leng, H. Li, Appl. Catal. B: Environ. 174–175 (2015) 445–454.
[45] B. Hu, F. Cai, T. Chen, M. Fan, C. Song, X. Yan, W. Shi, ACS Appl. Mater. Interfaces 7 (2015) 18247–18256.
[46] J. Di, J. Xia, M. Ji, B. Wang, S. Yin, Q. Zhang, Z. Chen, H. Li, Appl. Catal. B: Environ. 183 (2016) 254–262.
[47] C. Huang, W. Ye, Q. Liu, X. Qiu, ACS Appl. Mater. Interfaces 6 (2014) 14469–14476.
[48] X. Yang, F. Qian, G. Zou, M. Li, J. Lu, Y. Li, M. Bao, Appl. Catal. B: Environ. 193 (2016) 22–35.
[49] Y. Hong, Y. Jiang, C. Li, W. Fan, X. Yan, M. Yan, W. Shi, Appl. Catal. B: Environ. 180 (2016) 663–673.
[50] H. Wang, X. Yuan, H. Wang, X. Chen, Z. Wu, L. Jiang, W. Xiong, G. Zeng, Appl. Catal. B: Environ. 193 (2016) 36–46.
[51] X. Lv, J. Wang, Z. Yan, D. Jiang, J. Liu, J. Mol. Catal. A: Chem. 418–419 (2016) 146–153.
[52] D. Liu, Z. Jiang, C. Zhu, K. Qian, Z. Wu, J. Xie, Dalton Trans. 45 (2016) 2505–2516.
[53] J. Liu, Y. Song, H. Xu, X. Zhu, J. Lian, Y. Xu, Y. Zhao, L. Huang, H. Ji, H. Li, J. Colloid Interface Sci. 494 (2017) 38–46.
[54] Y. Hong, Y. Meng, G. Zhang, B. Yin, Y. Zhao, W. Shi, C. Li, Sep. Purif. Technol. 171 (2016) 229–237.
[55] J. Liu, H. Xu, Y. Xu, Y. Song, J. Lian, Y. Zhao, L. Wang, L. Huang, H. Ji, H. Li, Appl. Catal. B: Environ. 207 (2017) 429–437.
[56] L. Shi, L. Liang, J. Ma, F. Wang, J. Sun, Dalton Trans. 43 (2014) 7236–7244.
[57] B. Chai, X. Liao, F. Song, H. Zhou, Dalton Trans. 43 (2014) 982–989.
[58] Q. Liang, Z. Li, Y. Bai, Z. Huang, F. Kang, Q. Yang, Small 13 (2017) 1603182.
[59] S. Hu, L. Ma, F. Li, Z. Fan, Q. Wang, J. Bai, X. Kang, G. Wu, RSC Adv. 5 (2015) 90750–90756.
[60] L. Shi, L. Liang, F. Wang, M. Liu, J. Sun, RSC Adv. 5 (2015) 101843–101849.
[61] L. Cong, H. Mu, S. Zhang, M. Zhang, Z. Zhao, S. Fu, Nano 12 (2017) 1750042.
[62] A. Cai, Q. Wang, Y. Chang, X. Wang, J. Alloys Compd. 692 (2016) 183–189.
[63] X. Ding, K. Zhao, L. Zhang, Environ. Sci. Technol. 48 (2014) 5823–5831.
[64] H. Huang, X. Li, J. Wang, F. Dong, P.K. Chu, T. Zhang, Y. Zhang, ACS Catal. 5 (2015) 4094–4103.
[65] Z. Jia, F. Wang, F. Xin, B. Zhang, Ind. Eng. Chem. Res. 50 (2011) 6688–6694.
[66] J. Liu, Y. Liu, N. Liu, Y. Han, X. Zhang, H. Huang, Y. Lifshitz, S.T. Lee, J. Zhong, Z. Kang, Science 347 (2015) 970–974.
[67] M. Sun, S. Li, T. Yan, P. Ji, X. Zhao, K. Yuan, D. Wei, B. Du, J. Hazard. Mater. 333 (2017) 169–178.